Moon Imaging Technique and Experiments Based on Sanya Incoherent Scatter Radar

Mingyuan Li, Xinan Yue, Yonghui Wang, Junyi Wang, Feng Ding, Juha Vierinen, Ning Zhang, Zhongqiu Wang, Baiqi Ning, Biqiang Zhao, and Lingqi Zeng

***Abstract*— This article introduces the experiment design for Moon imaging based on Sanya incoherent scatter radar (SYISR) and algorithm research in data processing. The peak power of SYISR is 2 MW. The transmitted frequency used for Moon imaging experiments is 430 MHz. We conducted Moon imaging experiments using two types of waveforms, 13-bit Barker code, and linear frequency modulation (LFM) chirp. Considering both resolution and signal-to-noise ratio (SNR), the use of an LFM chirp with a bandwidth of 0.3 MHz and a pulsewidth of 2 ms can give higher SNR and resolution for Moon imaging using SYISR. Several key techniques were applied in the experiment design and data processing: 1) for the reliability of the imaging algorithm, the range-Doppler imaging algorithm commonly used in synthetic aperture imaging was applied; 2) to avoid the sidelobe effect of the 13-bit Barker code matched filter, a sidelobe-free filter was used; and 3) to mitigate the problem of "north–south ambiguity," mosaic imaging of the Doppler northern and southern hemispheres of the nearside of the Moon was adopted. Two types of imaging results are obtained: mosaic images of the northern and southern hemispheres of the Moon and local regional images. The results demonstrate the feasibility and reliability of Moon imaging based on SYISR, which enables potential further lunar geology investigations in the future.**

***Index Terms*— Moon, north–south ambiguity, range-Doppler (RD) map, Sanya incoherent scatter radar (SYISR).**

I. Introduction

RADAR technology developed rapidly during the Second World War. In the period since then, many ground-based radar systems (GBRs) have been used for planetary detection. The Moon, as the celestial body closest to the Earth, naturally became the first target of such studies. GBR detection is an effective remote probing method for the Moon and even for other celestial bodies in the Solar System. GBR has provided a large amount of valuable information about the physical properties of the lunar regolith for more than 60 years. For example, information on the Moon's surface and subsurface rock abundance, regolith thickness [1], [2], iron and titanium content [3], impact melt distribution [4], and the discussion about the possible presence of ice deposits [5], as well as a large-scale topographic map of the front side of the Moon [6], has been obtained.

In 1946, American military radar was used to detect the Moon. This was the first time humans sent radio waves to the Moon using GBR, and echoes were received after approximately 2.5 s. Since then, scientists have begun to study GBR imaging technology for the Moon. Early in this work, continuous wave and pulsed transmissions were used. Using continuous-wave detection, the value of the radar cross section (RCS) as a function of wavelength was studied. The typical cross section is approximately 7% of the geometrical cross section, and the wavelength dependence is very slight. When pulsed transmissions are used, the received power curve against delay can be measured. This indicates that the cross section is a function of the angle of incidence. The cross section is largest at a normal angle of incidence and decreases drastically as the incidence angle increases toward 90° [7].

The 1960s and 1970s were a period of great development in GBR detection technology for the Moon. Pettengill and Henry [8] at the Massachusetts Institute of Technology (MIT) developed the range-Doppler (RD) technique, which has been widely used in planetary radar remote sensing. This technique led to two GBR Earth-side Moon mapping experiments in the late 1960s. One was conducted at the Arecibo Observatory using a wavelength of 70 cm with a resolution of 15 km × 15 km. The other was conducted at the Haystack Observatory using a wavelength of 3.8 cm with a resolution of 2 km × 2 km [7]. Numerous articles were published based on these two observations and related work in the 1960s and 1970s. In particular, a series of four articles is highlighted here.

1) The first of these describes the RD technique and some details of the algorithms and measurements [9].
2) The second article describes the results of 70-cm wavelength measurement at Arecibo [10]. Both polarized (i.e., echoes polarized in the opposite circular sense as that transmitted are termed "OCP," and they are from quasi-specular or coherent scattering by the surface) and depolarized (i.e., echoes polarized in the same circular sense as that transmitted are termed "SCP," and they are from diffuse or multiple scattering by rocks on

Manuscript received January 19, 2022; revised March 14, 2022 and April 8, 2022; accepted April 8, 2022. Date of publication April 13, 2022; date of current version April 28, 2022. This work was supported in part by the B-type Strategic Priority Program of the Chinese Academy of Sciences under Grant XDB4100000 and in part by the Meridian Project and the National Natural Science Foundation of China under Grant 41427901. *(Corresponding author: Xinan Yue.)*

Mingyuan Li, Xinan Yue, Yonghui Wang, Junyi Wang, Feng Ding, Ning Zhang, Zhongqiu Wang, Baiqi Ning, Biqiang Zhao, and Lingqi Zeng are with the Key Laboratory of Earth and Planetary Physics, Institute of Geology and Geophysics, Chinese Academy of Sciences, Beijing 100029, China, also with the College of Earth and Planetary Sciences, University of Chinese Academy of Sciences, Beijing 100049, China, and also with the Beijing National Observatory of Space Environment, Institute of Geology and Geophysics, Chinese Academy of Sciences, Beijing 100029, China (e-mail: yuexinan@mail.iggcas.ac.cn).

Juha Vierinen is with the Department of Physics and Technology, The Arctic University of Norway, 9019 Tromsø, Norway.

Digital Object Identifier 10.1109/TGRS.2022.3167156

the surface or buried in the subsurface) echoes were received, and these echoes were used to generate lunar maps with a Moon surface resolution of approximately 5–10 km. The maps indicated that young craters have enhanced echoes and that a few craters only display echo enhancement from their rims. The backscattering power from highland areas is larger than that from Maria.

3) The third article describes the mapping of radar echoes at a wavelength of 3.8 cm at Haystack [11]. In that work, both OCP and SCP echoes were studied. At this short wavelength, surface roughness on centimeter-to-decimeter scale is the dominant source of diffuse echoes, compared to the decimeter-to-few-meter scales relevant to 70-cm observations.
4) The fourth article presents a more detailed analysis of a variety of lunar features based on the datasets and results reported in two of the above articles [12].

These four articles provided a theoretical foundation for follow-up work. In the 1970s, interferometry was applied to radar astronomy to produce topographic maps of the Moon [13], [14]. Interferometry provides a method for separating the echoes from two conjugate areas with respect to the apparent Doppler equator with the same delay and Doppler shift, an effect that is usually called "Doppler north–south ambiguity." Thompson [15] reported a lunar mapping result obtained at a wavelength of 7.5 m using interferometry to solve the problem of north–south ambiguity. If an interferometry technique cannot be adopted, a narrow beamwidth can be used to illuminate only a small area of the lunar surface to avoid north–south ambiguity, similar to the method used by Thompson [10] and Zisk *et al.* [11] in Arecibo 70-cm and Haystack 3.8-cm detection. However, a relatively wide beamwidth, such as the 0.5° beamwidth of the European Incoherent SCATter radar association (EISCAT) UHF radar, can also be used to illuminate only the northern or southern hemisphere of the Moon [16]. At the end of the 1970s, Thompson published a review of GBR mapping of the Moon [3]. He summarized radar mapping results obtained at the wavelengths of 3.8 cm, 70 cm, and 7.5 m.

During the 1980s and 1990s, some improvements in mapping technology were made. For instance, a new 70-cm mapping with a higher resolution of 2–5 km was obtained at the Arecibo Observatory due to its processing algorithm improvement [17]. In addition, some new wavelengths were adopted to perform detection. For instance, the Arecibo 12.6-cm wavelength radar system was used to image lunar polar regions with a resolution of 125 m for ice deposit searching [5].

From 2000 to the present, scientists have been constantly updating GBR lunar mapping technology and results. One result that must be noted is that Campbell *et al.* [18] presented a new 70-cm wavelength radar lunar map obtained via a patch-focusing method that greatly improved the resolution from 2–5 km to 450–900 m. The image coverage extended to areas near the poles and limbs that had not previously been investigated [18]. Campbell *et al.*'s [2] article is the first to take the 70-cm wavelength range resolution to the best-possible Arecibo 1-μs value, which corresponds to a surface spatial resolution of 200–250 m. Another more recent result was obtained at a 6-m wavelength using the Jicamarca Radio Observatory 50-MHz radar [19]. An interferometry technique was used to remove the north–south ambiguity. Both OCP and SCP echoes were investigated. Although a similar wavelength of 7.5 m has been used to map the Moon [15], this 6-m wavelength study provided an SCP scattering map, while the 7.5-m result did not, and the resolution of this 6-m result was 10–20 km, compared with the 30–40-km resolution obtained in previous 7.5-m work. There have also been some other important results in recent years. Campbell *et al.* [4], [18], [20], [21] reported some research on 12.5- and 70-cm wavelength mapping using the Arecibo Observatory and the Green Bank Telescope.

Since there have been numerous lunar orbiters (including multipolarimetric radars), landers, and rovers [22], why still use GBR data to explore the Moon? First, we should note that remote probing by GBR is much less costly than launching instruments to the Moon. In addition, GBR remote probing can provide information on a large area of the lunar surface in a relatively short time and can also detect lunar subsurface features that optical methods cannot [2], [21]. Another strong point is that no current orbital radar goes longward of L-band, so P-band GBR still has an advantage in probing depth. Furthermore, the Moon is not the only rocky object of interest for GBR, which can be used to study Venus, Mercury, Mars, and the asteroids [23]–[26]. For many years to come, GBR remote sensing will still play an important role in planetary research.

A high-power large-aperture phased array incoherent scatter radar system, Sanya incoherent scatter radar (SYISR), has recently been completed at Sanya (18.3°N, 109.6°E), a low-latitude station on Hainan Island, China. SYISR is a modular active phased array system. It uses all solid-state transmission and digital reception. It transmits right-handed circularly polarized electromagnetic waves and receives left-handed circularly polarized echoes (i.e., SYISR measures only the OCP echo). The radar has a peak power of approximately 2 MW, and the operating frequency is 430–450 MHz, which means that the wavelength is approximately 66.7–70 cm, similar to the wavelength of the Arecibo system used in previous work [18]. The system's total power with pulse modulation is powerful enough to observe the Moon.

This article introduces the Moon imaging experiments using SYISR, including key technology, experiment design, data collection, and data processing. The results show the ability of SYISR detecting and imaging the Moon and show the instrument has promise. However, for now, because only the OCP echo can be received, what SYISR can do for the lunar science is limited. In the future, after the hardware upgrade or collaborating with other powerful receive antenna, more lunar science research is possible.

II. Key Technology

We have applied some key technologies in SYISR Moon imaging experiments. Before introducing the details of the

experiment, we will briefly introduce these technologies in this section.

A. RD Technique

If the angular resolution of GBR is directly used to image the Moon, the result is very unsatisfactory. Even one as small as Arecibo's 9-arcmin beamwidth cannot be used to obtain a high angular resolution lunar map. However, the Moon is a rigid body, and every point on the lunar surface moves with the rotation and revolution of the Moon. Therefore, every surface point has a motion and generates a Doppler shift that is detectable by a GBR. Based on this idea, Pettengill and Henry [8] combined frequency and range resolution to create the well-known RD mapping technique. For a long time, this technique has been used with GBR to map the Moon and other celestial bodies such as Mars [23] and Venus [24]. In mapping of the Moon using this method, two simplifying assumptions are usually made. First, the Moon is assumed to be a sphere with a radius of 1738 km. Second, the parallax is assumed to be negligible. These assumptions introduce some errors, the magnitude of which is approximately 1 or 2 km.

The RD technique uses both the range and the Doppler frequency resolution to map a target. The range (time delay) resolution is determined by either the uncoded pulselength or the range-compressed results of a coded or chirped signal. The Doppler frequency resolution is obtained by the frequency spectrum analysis of the received radar echoes

$$\Delta R = c\tau/2 \tag{1}$$

$$\Delta A = \frac{R_{\text{moon}}\Delta f}{w} = \frac{\lambda \Delta f}{2\omega_a} = \frac{\lambda}{2\omega_a T} = \frac{\lambda}{2\Delta\theta}. \tag{2}$$

In (1) and (2), ΔR is the range resolution, ΔA is the azimuth resolution related to the Doppler frequency resolution $\Delta f = 1/T$, c is the speed of light, τ is the pulselength (for uncoded pulses), R_{moon} is the radius of the Moon, T is the coherent integration time used in the frequency spectrum analysis, $w = 2R_{\text{moon}}\omega_a/\lambda$ is the maximum Doppler shift of the lunar disk, $2w$ is the Doppler broadening of the lunar scattering signal, ω_a is the apparent angular rate of rotation of the Moon, λ is the radar wavelength, and $\Delta\theta$ is the angle through which the body turns during the coherent integration time.

The main goal of using GBR and the RD technique to map the Moon is to obtain an RD map in which each pixel represents an area on the lunar surface and the power strength of each pixel represents the sum of the echo strength from the area corresponding to that pixel. Such an RD map can be obtained by transmitting a string of pulses to the Moon at a certain pulse repetition frequency (PRF) and receiving the echo signal at a certain sampling rate. Next, the frequency-domain analysis is performed on the samples from a series of continuous pulses with the same delay (range). Finally, the signal is resampled from RD coordinates into selenographic coordinates. Campbell *et al.* [18] introduced the details of this coordinate transformation. The period of all the pulses used in the frequency-domain analysis is called the coherent integration time. The echo of all pulses in one integration time can be considered a coherent signal; this would indicate that the Moon's position and velocity remain unchanged during the scattering of these pulses. However, these parameters are not absolutely unchanged, and the changes may cause migration and defocusing. For this reason, compensation and focusing techniques are needed. Details concerning possible focus methods will be discussed later.

Now, let us discuss the geometry of RD radar mapping. Fig. 1 shows the geometry of GBR mapping the Moon from the front, side, and top views. A Cartesian coordinate system whose original point is located at the Moon's center of mass (COM) is employed. The X-axis points to the radar, the Z-axis extends along the apparent spin axis toward the north, and the Y-axis follows the right-hand rule. The subradar point (SRP) is the point at which the X-axis and the lunar surface intersect. The apparent Doppler equator is formed by the intersection of the XY plane with the lunar surface. This Cartesian coordinate system simplifies the analysis. The contours with constant delay (range) on the lunar surface form SRP-centered concentric circles that lie in planes perpendicular to the X-axis. The contours with constant Doppler shift on the lunar surface form stripes that lie in planes perpendicular to the Y-axis. Pettengill *et al.* [9] described the details of the relationship between RD coordinates and Cartesian coordinates.

During the observation period, the SRP moves on the lunar surface. This motion contains two components. One is the Moon's libration caused by the Moon's rotation and revolution. The other is the movement of the Moon's COM with respect to the radar due to the Earth's rotation and the Moon's revolution. Two successive COM-to-SRP vectors define the apparent Doppler equator plane, and the apparent spin axis is the vector perpendicular to the apparent Doppler equator plane at the COM pointing to the north.

B. Sidelobe-Free Filtering

For the GBR lunar imaging experiment, if a 13-bit Barker code is used for detection, the use of a matched filter (hereinafter referred to as MF) for decoding will blur the image due to the sidelobes. However, the application of sidelobe-free decoding filter (also known as inverse filters, hereinafter referred to as IF) can effectively avoid this problem.

The Barker code divides a pulselength into several baud lengths, and each baud is modulated by a phase of 0° (+1) or 180° (−1). After the echo is received, it must be decoded. An MF is usually used for decoding. In the MF method, the image code of the transmitted pulse envelope is used as the filter function to convolve the echo. Signals decoded in this way achieve the best signal-to-noise ratio (SNR). The range resolution depends on the baud length of the Barker code, and the signal intensity indicates the accumulated energy corresponding to the entire Barker code pulselength. Although the matched filtering performance of the Barker code is good, the problem of sidelobes is still present, and this interferes with target detection in some specific situations. For example, when a strong point target echo is detected, the sidelobes of the Barker code MF will spread the point target echo to

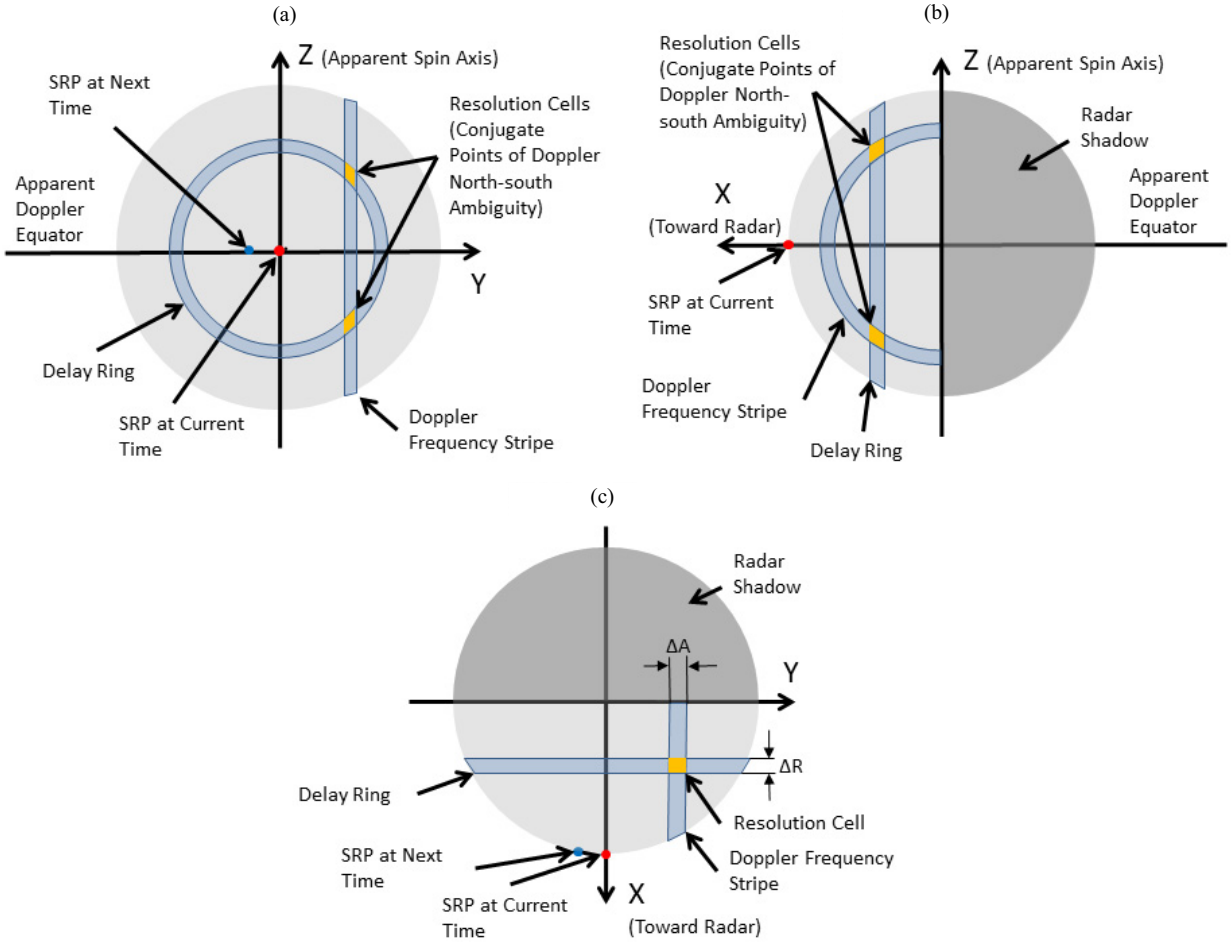

Fig. 1. Diagram showing the relationship between delay (range) and Doppler shift coordinate system and the lunar observation Cartesian coordinate system (X, Y, Z). (a) Front view (YZ plane). (b) Side view (XZ plane). (c) Top view (XY plane). ΔR and ΔA are related to (1) and (2), respectively.

the surrounding range gates. This makes the range resolution coarser than for a narrow impulse response.

There have been many studies of the sidelobe problem associated with the use of Barker code MFs. For example, a designed weighting network can be placed after the standard MF to effectively suppress the sidelobe effect [27]. The sidelobe effect can even be completely eliminated through the use of IFs [28]. Lehtinen *et al.* [29] applied the IF proposed by Sulzer to data analysis. However, Sulzer also mentioned that, unlike MF decoding, IF decoding cannot achieve the best SNR, and the degradation of the SNR depends on the encoding method [28]. In the case of a 7-bit Barker code, the SNR of IF decoding is nearly 30% worse than that of MF decoding. For a 13-bit Barker code, it is only approximately 5% worse [30]. However, IF can solve the sidelobe problem caused by the use of Barker code MFs, and if a 13-bit Barker code is used, the advantages of IF entirely compensate for the disadvantages caused by the deterioration of its SNR.

In the SYISR Moon imaging experiment, the first attempts used the 13-bit Barker code. The Moon echo can be regarded as the echo generated by a series of continuous point targets. Use of the Barker code MF will cause the sidelobe effect to produce obvious range ambiguity. This affects the range resolution. Therefore, to solve the sidelobe problem caused by MF, we attempted to use the IF decoding algorithm.

C. Mosaic Imaging of the Northern and Southern Hemispheres of the Nearside of the Moon

The technique of using the range-Doppler algorithm to image rotating celestial bodies has a flaw, which is the echoes at the two conjugate points of the northern and southern hemispheres on both sides of the apparent equator that cannot be distinguished in the RD image. This will result in overlapping of the southern and northern hemispheres and that is Doppler north–south ambiguity. For example, the two points in Fig. 1 that are labeled "conjugated points of Doppler north–south ambiguity" will cause this problem.

To solve this problem, we adopted Vierinen's method [16] and proposed a solution based on SYISR. This solution involves mosaic imaging of the northern and southern hemispheres of the nearside of the Moon. Two independent experiments are conducted in which the beam is adjusted to point to a specific position so as to illuminate either only the northern or only the southern hemisphere of the nearside of the Moon. Finally, a complete image of the Moon is obtained by creating a mosaic of the images of the southern and

northern hemispheres. The key part is how to control the beam direction. Actually, this method only can reduce the strength of the ambiguous points and cannot get rid of the ambiguity completely. This is because some unwanted echoes from sidelobes may still appear. The specific implementation process is introduced in Section III-C.

III. Experiment Design and Data Collection

We used two types of transmitted signal waveforms in the experiments: 13-bit Barker code and linear frequency modulation (LFM) chirp. Before performing the experiment, we simulated the SNR of the lunar echo; this is described in Section III-A. The specific experiment parameters and experiment design are introduced in Section III-B. The control of beam pointing is related to the mosaic imaging technique of the northern and southern hemispheres of the nearside of the Moon, and the technique is introduced in Section III-C.

A. SNR Estimation

According to the radar equation, the SNR of the SYISR monostatic detection of the lunar echo can be estimated, and this can help us design the experiment parameters. The radar equation used here is given as follows:

$$\mathrm{SNR} = \frac{P_t \varepsilon G^2 \lambda^2 \sigma \tau B_w}{(4\pi)^3 R^4 \kappa T_s B_r L_s} \tag{3}$$

where $P_t = 2$ MW is the peak transmit power, ε is the duty cycle, $\varepsilon = 3\%$ for both the 13-bit Barker code experiment and the chirp experiment, $P_t\varepsilon$ is the average transmit power, $G = 43$ dB is the antenna gain, $\lambda \approx 70$ cm is the radar wavelength, $\sigma = (0.081 \pm 0.005)\pi R_{\mathrm{moon}}^2 \approx 1.0428 \times 10^{12}$ [31] is the RCS of the whole Moon disk, $R_{\mathrm{moon}} = 1737.1$ km is the average radius of the Moon, τ is the pulselength ($\tau = 390$ μs in the 13-bit Barker code experiment and $\tau = 2$ ms in the chirp experiment), B_w is the bandwidth of the waveform ($B_w = 0.03$ MHz in the 13-bit Barker code experiment and $B_w = 0.3$ MHz in the chirp experiment), τB_w is the gain from pulse compression, $R = 3.844 \times 10^5$ km is the estimated average distance from the radar source to the COM of the Moon, κ is Boltzmann's constant, $T_s = T_a + T_i = 244$ K is the system noise temperature, $T_a = 124$ K is the antenna noise temperature, $T_i = 120$ K is the noise temperature inside the system, $B_r = 0.4$ MHz is the receiver bandwidth, and $L_s = 5.5$ dB is the system loss. Substituting these parameters into (3), the lunar echo SNR can be calculated as approximately 29 dB for the 13-bit Barker code experiment and 45 dB for the chirp experiment. The SNR calculated here is used to analyze whether the SYISR performance supports the detection of the Moon. Thus, it is only an initial result. If calculating the SNR of mapping pixels, the RCS here is overestimated because the factors (such as the area of resolution cells and the antenna pattern) that influence the mapping pixel RCS should be considered.

In the case described above, the radar beam points to the COM of the Moon. However, when using SYISR to image the Moon, it is necessary to place the beam only on the position that illuminates either the southern hemisphere or the northern hemisphere to avoid the issue of north–south ambiguity. In this case, the effective antenna gain G decreases to 32 dB, and the RCS decreases to $\sigma \approx 5.2139 \times 10^{11}$. The SNR of the lunar echo is 25 dB lower than that of the COM detection. However, in general, SYISR can still detect the Moon echo well after coherent integration.

TABLE I
Experiment Parameters

Parameter	13-bit Barker code Experiment	Chirp Experiment
Peak transmit power	2 MW	2 MW
Antenna gain	43 dB	43 dB
Pulse length	390 μs	2 ms
Baud length or bandwidth	30 μs	0.3 MHz
Pulse repetition frequency	76.92 Hz	16.67 Hz
Pulse repetition time	13 ms	60 ms
Coherent integration period	~60 s	~240 s
Sample period	10 μs	10 μs
Range resolution	~4.5 km	~0.5 km
Azimuth resolution	~4.8 km	~1.2 km
Sample number for FFT	8192	4096

B. Experiment Parameters

It is necessary to set reasonable experiment parameters before performing lunar imaging experiments. The relevant parameters include waveform parameters, coherent integration time, PRF, and some others. The specific parameter settings are shown in Table I.

Pulsed electromagnetic waves were transmitted in the experiments. The waveform parameters include the type of waveform and its pulselength, baud length, and bandwidth. Two factors should be considered in selecting the parameters: one is that the pulselength should be wide enough for the echo to have a sufficient SNR, and the other is that the bandwidth is sufficiently large to allow considerable range resolution after pulse compression. Considering these two factors, a 13-bit Barker code is initially selected as the transmission waveform, and a pulsewidth of 390 μs and a baud width of 30 μs are used; the corresponding range resolution is 4.5 km. Due to the limited baud number of the Barker code, the baud width needs to be reduced to improve the range resolution. This means that the SNR will be sacrificed. In our experiment, we also used an LFM chirp to solve this problem. With a pulsewidth of 2 ms and a bandwidth of 0.3 MHz, the theoretical range resolution can reach 500 m. In this way, a high SNR can be ensured, and an ideal range resolution can be obtained.

The coherent integration time affects the Doppler resolution of the RD map, and it can also be said that it affects the azimuth resolution of lunar imaging. As shown in (2), a longer coherent integration time can provide higher azimuth

resolution, but the Allen deviation σ_a of the radar clock defines the upper limit of the coherent integration time $t = (8\omega\sigma_a)^{-1}$, where ω is the radar frequency. If this time is exceeded, coherence will be lost, and the quality of the imaging will deteriorate [16]. At present, SYISR is equipped with a crystal oscillator clock that can provide a coherent integration time of approximately 290 s; this means that the azimuth resolution can reach approximately 1 km. However, we decided to use the coherent integration times of approximately 60 s for the 13-bit Barker code experiment and 240 s for the chirp experiment. There were two factors we considered. One was to make the azimuth resolution comparable to the range resolution. The other was to avoid exceeding the maximum defined by the clock.

The PRF should be chosen according to the limits of range and Doppler aliasing. It must satisfy the condition $2w \leq \text{PRF} \leq 1/\Delta t_{\max}$, where w is the maximum Doppler shift of the lunar echo signal and $\Delta t_{\max}$ is the maximum delay depth for the pulse going through the lunar nearside hemisphere. Thus, it is a range of approximately 12 Hz $<$ PRF $<$ 86.3 Hz, and the pulse repetition time (PRT, i.e., the inverse of PRF) should be 83.3 ms $>$ PRT $>$ 11.6 ms. Here, 11.6 ms is the delay depth of the lunar echo, and 12 Hz is the approximate Doppler broadening of the lunar echo at a wavelength of 70 cm [18]. These conditions can be interpreted as: 1) sampling the frequency-broadened echo from the Moon at the relevant Nyquist frequency to avoid Doppler ambiguity and 2) not allowing the PRT to exceed $\Delta t_{\max}$ to avoid range ambiguity between successive pulses. In addition, in actual experiments for monostatic radar lunar imaging, it is necessary to carefully select an appropriate pulse repetition period so that the lunar echo does not overlap with the transmission time [16].

C. Beam Pointing Control

During each experiment, the beam was controlled to track the Moon for 30 min. The beam was adjusted every 5 s to maintain tracking of the Moon. The first 15 min were used to illuminate the northern hemisphere, and the latter 15 min were used to illuminate the southern hemisphere. The key to this method is how to accurately and reasonably control beam pointing to realize the mosaic imaging technique. The following describes some details of the specific implementation.

1) Use Antenna Pattern to Define Beamwidth: First, to accurately control the beam, it is necessary to estimate the beamwidth of the SYISR. The method used here is to measure the width of the main lobe of the beam through the antenna pattern. There are two ways to obtain the antenna pattern. One is to use the radar's internal monitoring system to monitor the antenna pattern. The other is to simulate the antenna pattern based on antenna theory and consider the parameters of the radar. Under the ideal conditions of full power and trouble-free operation, the monitored pattern and the theoretical simulation pattern should be basically the same, and the slight difference can be ignored. Therefore, for simplicity, we adopted the second method.

The SYISR normalized antenna pattern is simulated according to the phased array antenna pattern formula [32] given by the antenna theory, and the beam is set to point in the zenith direction. The SYISR antenna array is arranged in a triangular grid with a north–south interval of 0.38 m and an east–west interval of 0.5 m. The transmission frequency during the experiment is 430 MHz. These parameters determine the calculation of the pattern.

TABLE II
ENERGY ILLUMINATING THE OBSERVED HEMISPHERE AND THE UNOBSERVED HEMISPHERE USING DIFFERENT BEAMWIDTH DEFINITIONS

Beam width definition	3-dB beam width (1.08°)	10-dB beam width (1.8°)	The first null beam width (2.44°)
Percentage of the energy on observed hemisphere to the total energy of the main lobe (P_{obs})	4.31%	1.08%	0.23%
Percentage of the energy on unobserved hemisphere to the total energy of the main lobe (P_{unobs})	1.68%	0.33%	0.05%
P_{obs} to P_{unobs} ratio	2.57	3.22	4.84

There are two commonly used ways to define the beamwidth. The first is the half-power beamwidth (3-dB beamwidth); for SYISR, its value is approximately 1.08°. Approximately 71.31% of the energy is included in the 3-dB beamwidth. This method of calculating the beamwidth can be applied in most situations. However, approximately 28.69% of the energy is distributed outside the 3-dB beamwidth. Another way to define the beamwidth is as the first null beamwidth. The first null beamwidth, which is approximately 2.44° in SYISR, is the beamwidth defined using the edge of the beam when the peak energy of the main lobe is attenuated to 0. The beamwidth defined in this way includes all the energy of the main lobe within the beamwidth, and only the sidelobes are outside it.

When illuminating only the northern or southern hemisphere, strictly speaking, the echo of the other hemisphere cannot be received. Therefore, considering the use of the first null beamwidth from this aspect is optimal. Vierinen and Lehtinen [16] used the first null beamwidth of the EISCAT UHF radar to image the Moon. However, the first null beamwidth of the SYISR is 2.44°, wider than the field-of-view angle of the lunar diameter of 0.5°. This will cause a large amount of the energy of the main lobe beam to be wasted when only the northern or southern hemisphere is illuminated. Therefore, the received SNR is relatively low, and this affects

the imaging quality. To solve this problem, we adopted a compromise solution, taking the 10-dB beamwidth (approximately 1.8°) between the half-power beamwidth and the first null beamwidth as the final choice. The 10-dB beamwidth is defined using the edge at which the peak energy of the main lobe is attenuated to 10%. The 10-dB beamwidth includes approximately 93.85% of the energy of the main lobe. To illustrate the reasons for using this compromise solution more clearly, we simulated the relative magnitudes of the energy illuminating the observed hemisphere and the unobserved hemisphere when different beamwidth definitions are used. The simulated relative magnitudes are shown in Table II. The percentage of the energy illuminating on both observed and unobserved hemispheres to the total energy of the main lobe attenuates as the width of the defined beam increases, but their rates of attenuation differ. What we wish to do is to maximize the energy that illuminates the observed hemisphere as much as possible and minimize the energy that illuminates the unobserved hemisphere. The third row in Table II shows the ratio of the energy illuminating on observed hemisphere to unobserved hemisphere. A higher value means that the energy illuminating the observed hemisphere accounts for a higher proportion of the total echo energy. The simulated result shows that the ratio is lower when the 3-dB beamwidth is used, a situation that is not conducive to avoiding the problem of north–south ambiguity. When the first null beamwidth is used, although the ratio is highest, the energy illuminating the observed hemisphere accounts for only 0.23% of the total energy of the main lobe. This will make the SNR relatively weak. The use of a 10-dB beamwidth ensures that the observed hemisphere is illuminated by as much energy as possible (1.08% of the total energy of the main lobe); this will cause the SNR to satisfy the imaging needs. It can also avoid illuminating the other hemisphere so much as to cause serious north–south ambiguity. However, we have to accept the fact that there still will be a slight north–south ambiguity, especially near the apparent Doppler equator.

2) Distinguish the Northern and Southern Hemispheres and Illuminate Them Separately: To distinguish the northern and southern hemispheres during the imaging process, it is first necessary to locate the apparent equator. Two SRPs obtained at consecutive times, together with the lunar COM, define the apparent equatorial plane, and the great circle described by the intersection of the equatorial plane with the surface of the Moon is the apparent equator. The position of the SRPs on the lunar surface at the current time and the next time (e.g., after 5 s) and the lunar COM can be calculated by ephemeris.

When the apparent equator has been located, the northern and southern hemispheres can be distinguished according to the definition of the equator. The direction of the apparent axis of rotation can also be calculated. To calculate the direction of the beam that illuminates only the northern or the southern hemisphere, it is first necessary to obtain the beam direction from the radar to the lunar COM according to the ephemeris and then offset the angle by half the beamwidth to the south or north along the direction of the apparent axis of rotation. When tracking the Moon, the above calculation steps are repeated at every interval (e.g., 5 s) to obtain the time sequence of the beam directions to the northern and southern hemispheres.

All of the above calculations rely on accurate ephemeris. We used ephemeris data published on the Internet by the Jet Propulsion Laboratory (JPL) of National Aeronautics and Space Administration (NASA) (https://naif.jpl.nasa.gov/naif/data.html). The DE435 version was used for the Moon. The time coverage is from 00:00 on December 21, 1549, to 00:00 on January 25, 2650. Libration is considered in the process of using ephemeris data.

3) Mosaic Image of the Northern and Southern Hemispheres: The RD imaging algorithm can be roughly divided into two steps. In the first step, the echo signal in the time domain is segmented into the 2-D space of range and Doppler. In the second step, the image in the RD domain is projected onto the real lunar coordinate system, which can be a Cartesian rectangular coordinate system or a lunar projection coordinate system. In the first step, the echo signals from the southern or northern hemisphere are processed in the same way, but they need to be distinguished in the second step. To do this, the 2-D image in the RD domain is projected onto the Cartesian rectangular coordinate system, as shown in Fig. 1. If it is the image of the northern hemisphere, the Z-axis is set to a positive value; if it is the image of the southern hemisphere, it is set to a negative value. In this way, the images of the northern and southern hemispheres can be mosaicked in the same coordinate system. The resulting image completely covers the positive and negative semiaxes of the Z-axis, thus forming a complete image of the Moon. Later, if it is necessary to display the image in other coordinate systems, coordinate conversion is performed based on the geometric relationship.

IV. Data Processing

This section introduces the data processing method in detail.

A. Correction for the Time-Varying Range and Range Rate

Before generating the lunar RD map, we corrected the range and range rate variation of the lunar COM in the echo to preserve the range and Doppler information of each point on the lunar surface referring to the lunar COM. In this way, the signal can be segmented into a 2-D RD image. The three corrected parts include the offset of the range gates caused by the range variation, the phase difference caused by the range variation shown in (4), and the Doppler shift shown in the following equation:

$$\Delta\emptyset_R(t_n) = \exp(2\pi j * 2\Delta R(t_n)/\lambda) \tag{4}$$

$$\Delta\emptyset_D\left(t_n, t_{\text{delay}}\right) = \exp\left(2\pi j * f(t_n) * t_{\text{delay}}\right). \tag{5}$$

In (4) and (5), $\Delta R(t_n)$ and $f(t_n)$ represent the range migration and the Doppler shift of the lunar COM, respectively, at time t_n of the beginning of the nth PRT, and t_{delay} represents the delay during one PRT.

The RD image obtained in this way is an unfocused map. For each point on the lunar surface, the range to the lunar COM and the Doppler information are still changing over time. When the coherent integration time is too long, the actual range or Doppler variation exceeds the specified range

or the Doppler resolution, and the image will be blurred. For the SYISR LFM chirp experiment in this article, if coherent integration time reaches 250 s, range variation will exceed the range resolution and the blurred region will occur near the Y-axis limb. The degree of blur will increase and the blurred region will expand from the Y-axis limb to the Y-axis center as coherent integration time increase. When the coherent integration time reaches 360 s, Doppler variation will exceed the Doppler resolution and another blurred region will occur near the SRP. Then, as coherent integration time increases, the degree of blur will increase and the blurred region will expand from SRP to the Moon disk limb. Focusing technology can solve this problem. However, in this article, there is no need to use it when the coherent integration time is less than 250 s. Thus, we will not further discuss the focusing algorithm for now. If in follow-up work, the resolution requirements increase, then the longer integration time will lead to a need to focus on the dataset.

B. Calibration of the Echo Power

The intensity of the lunar echo is determined by many factors, including the incident angle of the radar wave, the area of the scattering element, the antenna pattern, the lunar surface and subsurface rock abundance (roughness), and other factors related to the scattering characteristics. Because the influences of the first three factors are not very helpful in studying lunar geology, they should be corrected for during the imaging process. The effects of the other factors have a value in research on lunar geology and need to be retained in the image.

The following is a detailed introduction to the calibration process.

1) Correcting the Influence of Radar Wave Incidence Angle: The method is using the average normalized curve of the OCP echo power with the incidence angle when the 68-cm radar wave detects the Moon [7] to correct the measured echo. The calibration curve is shown in Fig. 2(a). The blue curve represents the averaged data obtained during 15 min of tracking and observing the southern hemisphere of the Moon. The red points represent data from a previously published article [7], and the black curve is the fitting curve of the red points. Equation (57) in Hagfors' article [7] was used to fit the portion of the incident angle that is less than or equal to 20°, and the portion of the incident angle greater than 20° was fitted to a fourth-order polynomial. The measured data are in good agreement with the data presented in Hagfors' article [7]. Finally, we used the black curve for correction.

2) Correcting the Influence of the Area of the Scattering Element: The area of the scattering element is calculated by projecting the RD 2-D resolution units onto the lunar surface and calculating the projected area. The result is shown in Fig. 2(b). When calibrating, the distribution of the scattering element area in Fig. 2(b) is first normalized and then used to correct the RD map.

3) Correcting the Influence of the Antenna Pattern: First, the elevation angle and the azimuth angle of each measured point on the lunar surface are calculated in radar local coordinates with the help of the ephemeris. Next, the normalized antenna pattern value at each point on the lunar surface is calculated according to the direction obtained in the previous step. The pattern is then projected onto the lunar surface to obtain the antenna pattern distribution on the lunar surface, as shown in Fig. 2(c). Finally, the lunar map is corrected to eliminate the effect of antenna pattern.

C. Boundary Identification

Before projecting the RD map onto the lunar projection coordinate system, we applied a boundary identification technique to identify the lunar echo boundary in the RD map. Actually, echo boundary here is a metaphor. It is the maximum frequency extent of the lunar echo at a particular range gate in the RD image. By identifying the boundary, the lunar apparent rotation angular velocity ω_a can be fitted according to (6). ω_a is very important for subsequent coordinate projection

$$\mathrm{BW}(r) = 4\omega_a \sqrt{R_{\mathrm{moon}}^2 - (R_{\mathrm{moon}} - r)^2}/\lambda. \tag{6}$$

In (6), $\mathrm{BW}(r)$ is the lunar echo bandwidth at each range gate and λ is the radar wavelength.

The boundary identification process is given as follows. First, a combination of image expansion and erosion techniques is used to sharpen the boundary of the Moon. A rectangular detection window is then created using the left half of -1 and the right half of $+1$, and a 2-D convolution with the lunar RD map is performed. This method will show the difference between the left and right pixel values within the local area determined by the rectangular detection window. After the convolution, the positions of the maximum and minimum values in each row of the image will be regarded as the left and right boundaries of the lunar echo. The specific parameters, such as the size of the rectangular detection window, are empirical values. Therefore, this boundary identification technique has certain errors, and this will cause a small portion of the noise outside the boundary to be mistakenly introduced into the lunar echo region.

If there is no error in the boundary identification, the apparent equatorial area will also have poor resolution due to the RD imaging technology. However, within a single month, the apparent equator moves slowly on the lunar surface. The defects regarding the apparent equator can be compensated for by observing the Moon on different dates within the same month. However, because the area near the SRP is always in an area in which the resolution is poor, it cannot be corrected in this way.

D. Coordinate Projection

The coordinate projection is divided into two parts. The first part is the projection from the RD domain $m(r, f)$ to the observation Cartesian coordinate system $m(X, Y, Z)$ shown in Fig. 1. The calculation equations are given as follows:

$$X = R_{\mathrm{moon}} - (r - r_0) \tag{7}$$

$$Y = \lambda \cdot (f - f_0)/(2\omega_a) \tag{8}$$

$$Z = \pm\sqrt{{R_{\mathrm{moon}}}^2 - X^2 - Y^2} \tag{9}$$

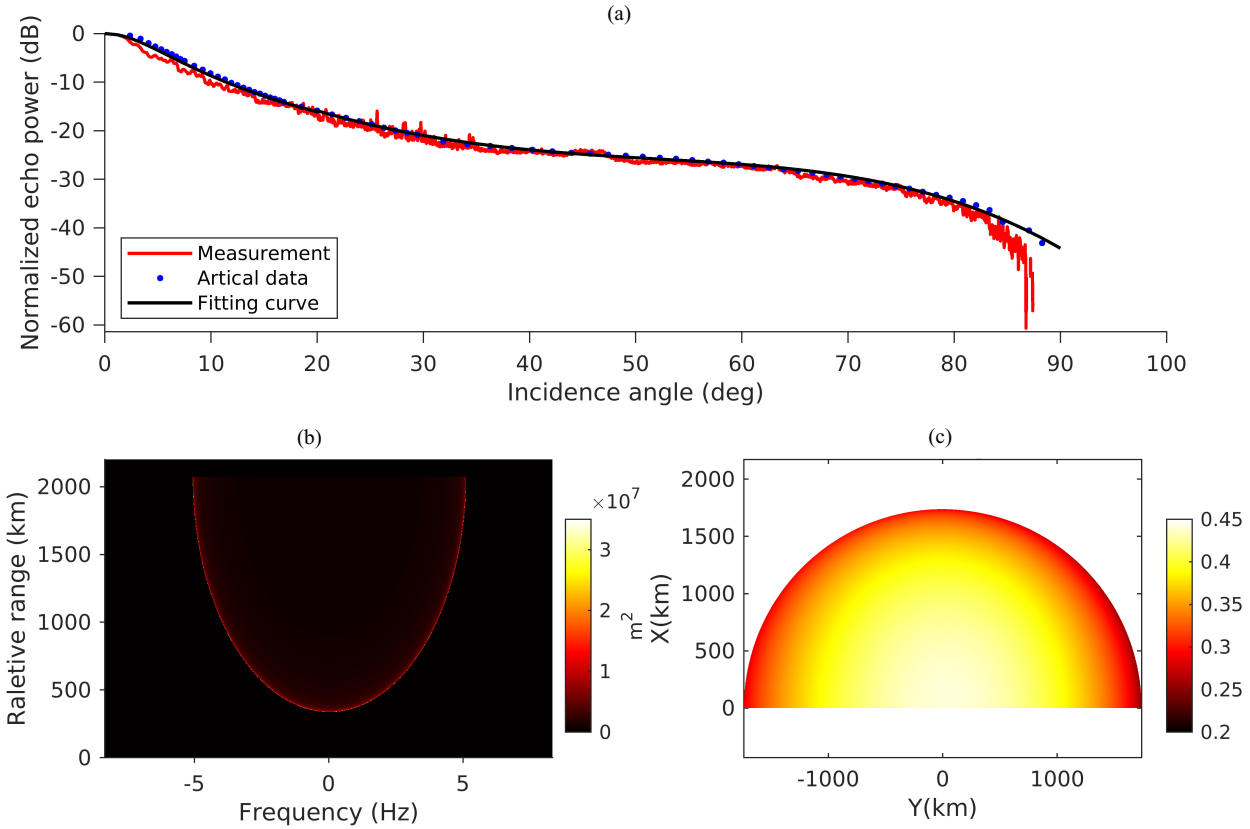

Fig. 2. Three factors that influence the echo power. (a) Curves showing OCP echo power corrected for the angle of incidence. The red curve is the average curve of the observation data from 01:30 to 01:45 local time in Sanya on February 7, 2021. The blue points show the data obtained by 68-cm wavelength radar detection presented by Hagfors (1970), and the black curve is the fitting curve of the blue points. The fitting curve was used for calibration. (b) Area of the scattering element in the RD domain. The map shown is a theoretical map calculated from the projection area of the 2-D RD resolution unit on the lunar surface. (c) Distribution of the normalized antenna pattern on the observed hemisphere of the nearside of the Moon. The distribution was calculated based on the ephemeris at 01:32:11 local time in Sanya on February 7, 2021, with a radar beam elevation angle of 45.16° and an azimuth angle of 196.11°. It is used to correct the images accumulated during the 4 min from 01:30:11 to 01:34:11 local time. (a) Normalized OCP echo power with the incidence angle. (b) Area of the scattering element (RD region). (c) Normalized antenna pattern (*XY* plane).

where R_{moon} is the lunar apparent equatorial radius (1738 km), r and r_0 are the range values of the projection point and the SRP, respectively, f and f_0 are the Doppler shift values of the projection point and the SRP, respectively, λ is the radar wavelength, and ω_a is the apparent angular velocity of rotation of the Moon. The value of ω_a is fitted by the boundary identification process. Z is a positive value when observing the northern hemisphere and a negative value when observing the southern hemisphere.

The second part of the coordinate projection is the projection from the observation coordinate system $m(X, Y, Z)$ to the lunar projection coordinate system $m(\text{lon}, \text{lat})$. The calculation method has been introduced in detail in Campbell's article [18].

E. Interpolation and Multilook Averaging

Each RD image obtained from one coherent integration time can be called one "look." Multilook averaging was used to reduce the variance due to noise in the lunar map. However, the observation geometry of every look is different. This leads to disunity of the longitude and latitude grids of the looks. Therefore, we linearly interpolate each look into a unified longitude and latitude grid before conducting multilook averaging. After the interpolation process, all the northern and southern hemisphere images are averaged, respectively, for each pixel in the unified longitude and latitude grid. Finally, the multilook averaged northern and southern hemisphere images were mosaicked to obtain a complete lunar map.

Actually, in the multilook averaging process, the accuracy of overlaying the features at the same position will be influenced by the latitude/longitude position error arising from boundary identification mentioned in Section IV-C. For local area imaging, to solve the ambiguity caused by the position deviation from the boundary identification error, we propose a method of searching the match window to correct this deviation. In this method, the first local image that needs to be averaged is taken as the target window. We then expand the search regions at the same position in every subsequent image and search for match windows within the search regions. After the match windows in all images are found, all the match windows are averaged with the target window, and the final multilook averaging result is obtained. The criterion for finding the match window is finding the largest 2-D correlation coefficient; the specific process can be found in the work of Yu *et al.* [33].

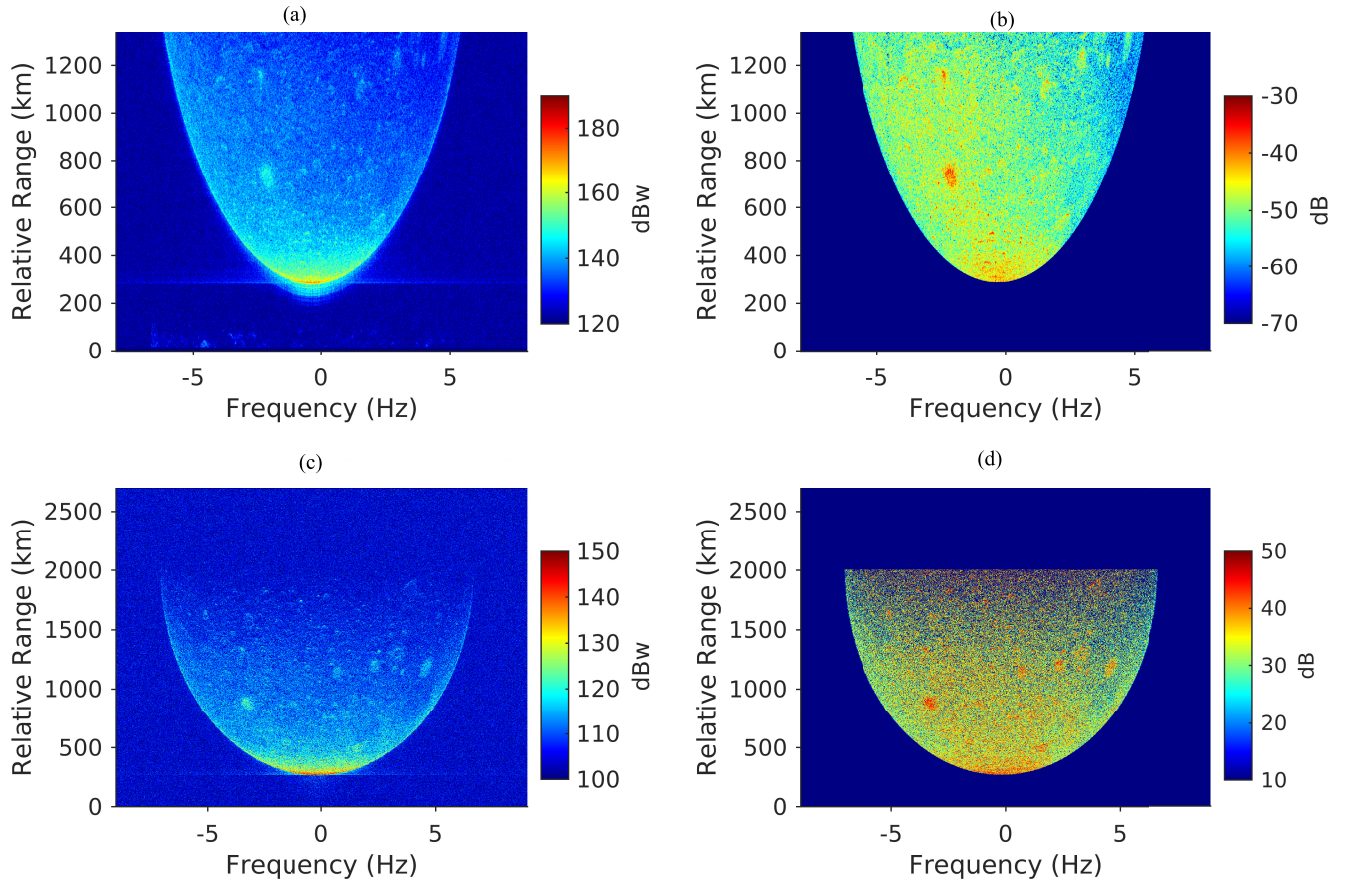

Fig. 3. RD maps of the southern hemisphere of the nearside of the Moon. (a) 13-bit Barker code RD lunar map using the IF decoding algorithm. It is the result before the calibration processing. (b) 13-bit Barker code RD lunar map using the IF decoding algorithm. It is the result after the calibration processing. (c) LFM chirp RD lunar map before the calibration processing. (d) LFM chirp RD lunar map after the calibration processing. (a) and (b) Results during 23:17–23:19 LT on December 29, 2020. (c) and (d) Results during 14:45–14:49 LT on March 16, 2021. (a) Barker code RD map (before calibration). (b) Barker code RD map (after calibration). (c) LFM chirp RD map (before calibration). (d) LFM chirp RD map (after calibration).

V. Results and Discussion

A. RD Images Obtained Using the 13-Bit Barker Code and the LFM Chirp

Fig. 3 shows the lunar RD images obtained using the 13-bit Barker code and the LFM chirp. Fig. 3(a) and (b) shows the 13-bit Barker code results using the IF decoding algorithm. Fig. 3(c) and (d) shows LFM chirp results. Fig. 3(a) and (c) shows the RD images before the calibration process. The frequency extent of the lunar echo at different range gates forms an arc in the RD image. This arc represents the apparent Doppler equator. The surface resolution cell near arc region is very large. This leads to the larger echo intensity compared to other areas. The top of the arc represents the position of the SRP. Since the incident angle of the electromagnetic wave near the SRP is close to normal, the echo intensity at SRP is much larger than that in other areas. In addition, the antenna pattern can also influence the distribution of echo intensity on lunar surface, though it is not obvious in Fig. 3(a) and (c) and Fig. 3(b) and (d) shows the RD images after the calibration process. Through the calibration process, the variance in the echo intensity mentioned above is corrected.

The sidelobe effect of 13-bit Barker code MF spreads the target echo in the range direction and pollutes other surrounding range gates, and previous research proves that IF can effectively reduce the sidelobe effect [28], [29]. However, in Fig. 3(a), the IF result still has some pollution in the range direction, especially near the SRP area outside the arc boundary. We compared the pollution of MF and IF results and find that the IF method reduces the MF sidelobe pollution by approximately 30%. Actually, in the coordinate projection step, the area outside the arc boundary will be cutoff. Therefore, there is no need to worry about the degree of pollution outside the boundary. In summary, although the sidelobe pollution is not eliminated completely, the use of the 13-bit Barker code IF decoding method in GBR lunar imaging experiments can indeed reduce the sidelobe pollution caused by MF decoding and improve the lunar imaging range resolution. IF decoding is also helpful in the case of other forms of two-phase encoding. In subsequent SYISR lunar imaging experiments, we will design a two-phase encoding technique with longer pulselength and higher resolution and adopt IF decoding methods. This has the potential to greatly improve the quality of lunar imaging.

B. Mosaic Imaging Results

When RD maps of the northern and southern hemispheres are together projected into a lunar observation Cartesian coordinate system, a mosaic image can be obtained. Fig. 4 shows

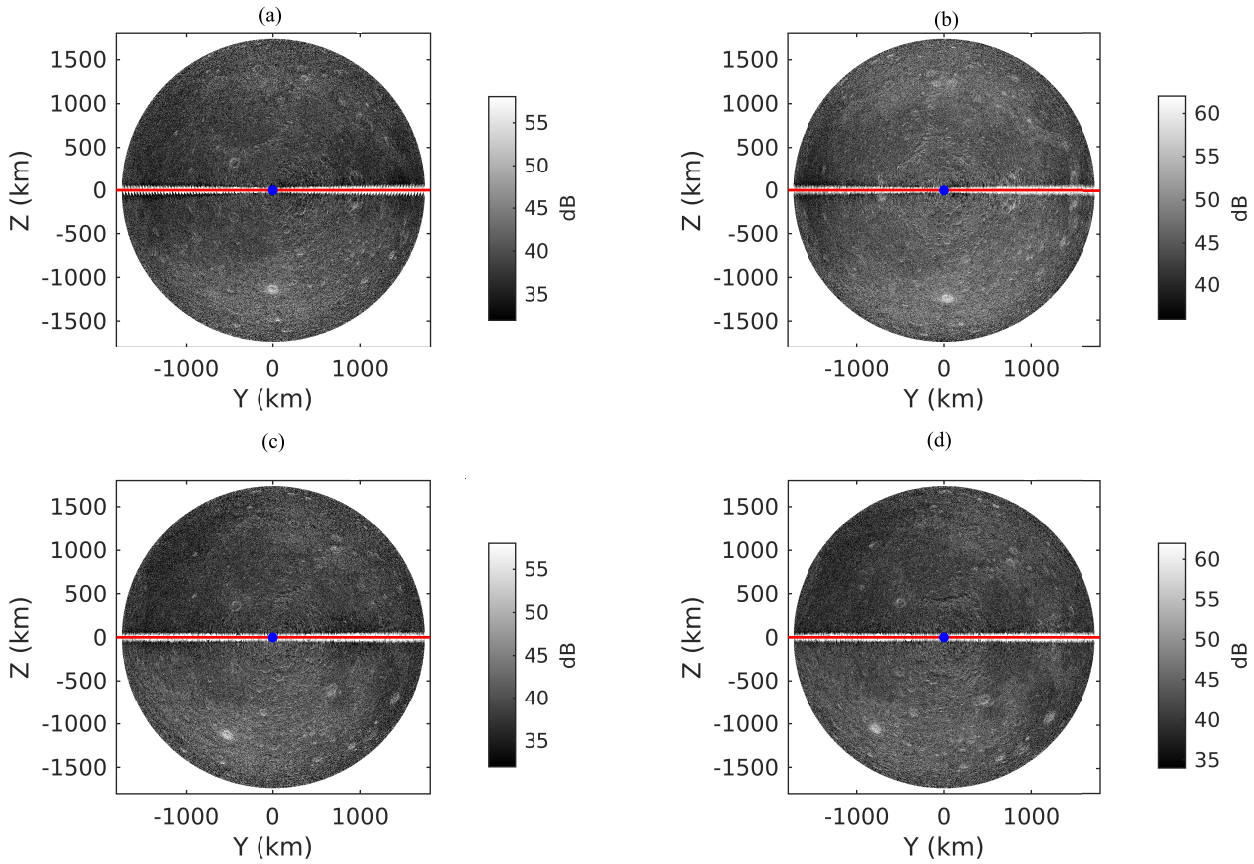

Fig. 4. Mosaic images of the northern and southern hemispheres of the nearside of the Moon. They are LFM chirp results. They are in the *YZ* plane of the lunar observation Cartesian coordinate system. They are from different experiment data on different dates. (a) One-look result during 01:00–01:30 LT on January 27, 2021. (b) One-look result during 09:15–09:45 LT on February 7, 2021. (c) One-look result during 19:15–19:45 LT on February 19, 2021. (d) One-look result during 14:30–15:00 LT on March 16, 2021. The red line represents the apparent equator, and the blue point represents the SRP. Near the red line, there is still a slight "north–south ambiguity" due to the second problem of the mosaic technique we used mentioned in Section V-B. (a) January 27, 2021, lunar image (*YZ* plane). (b) February 7, 2021, lunar image (*YZ* plane). (c) February 19, 2021, lunar image (*YZ* plane). (d) March 16, 2021, lunar image (*YZ* plane).

four mosaic images of the northern and southern hemispheres of the nearside of the Moon. The data used to construct these images were obtained in four chirp experiments that were conducted on four different local times and dates, and they are 01:00–01:30 local time on January 27, 2021, 9:15–9:45 local time on February 7, 2021, 19:15–19:45 local time on February 19, 2021, and 14:30–15:00 local time on March 16. 2021. The coordinate system in Fig. 4 is the *YZ* plane in the observation Cartesian coordinate system shown in Fig. 1(a). The results show that the main geological and geomorphological features of the northern and southern hemispheres are well presented, reflecting the feasibility and reliability of data processing.

In fact, the mosaic imaging technique we currently use still has some disadvantages.

The first problem is that regardless of where the beam is directed during the experiment, the beamwidth used for beam control is selected to be a fixed value in the zenith direction. However, for phased array radar such as SYISR, the beamwidth is not fixed. Generally, the lower the elevation angle is, the wider the beamwidth will be. This means that when tracking the northern or southern hemispheres of the Moon, the angle that deviates from the lunar COM direction should be adjusted as the elevation angle changes. However, this effect is temporarily ignored to reduce the computational complexity. In subsequent work, this will be a problem that needs to be traded off. On the one hand, it is necessary to estimate whether ignoring the variance in beamwidth will have a significant effect on imaging. On the other hand, it is necessary to estimate how much computational complexity will increase if the variance is considered. The beamwidth must be calculated each time the beam direction is changed.

The second problem is that the compromise choice of using a 10-dB beamwidth for the experiment design is flawed. A 10-dB beamwidth is adopted to avoid north–south ambiguity and to obtain sufficient SNR. In fact, the energy outside the 10-dB beamwidth and inside the first null beamwidth may still cause north–south ambiguity. In Fig. 4, a mirror-like feature exists near the apparent Doppler equator (denoted by the red line) in each mosaic image. It is north–south ambiguity caused by the energy outside the 10-dB beamwidth. In addition, SYISR can only illuminate the lunar southern or northern hemisphere using energy within the 10-dB beamwidth and outside the 3-dB beamwidth. The energy within the 3-dB beamwidth is completely wasted. Therefore, the performance of the radar has not been fully utilized. The fundamental reason for this situation is that the beamwidth of the SYISR is still too wide for lunar exploration. However, interference technology can better solve this problem. Two antennas are

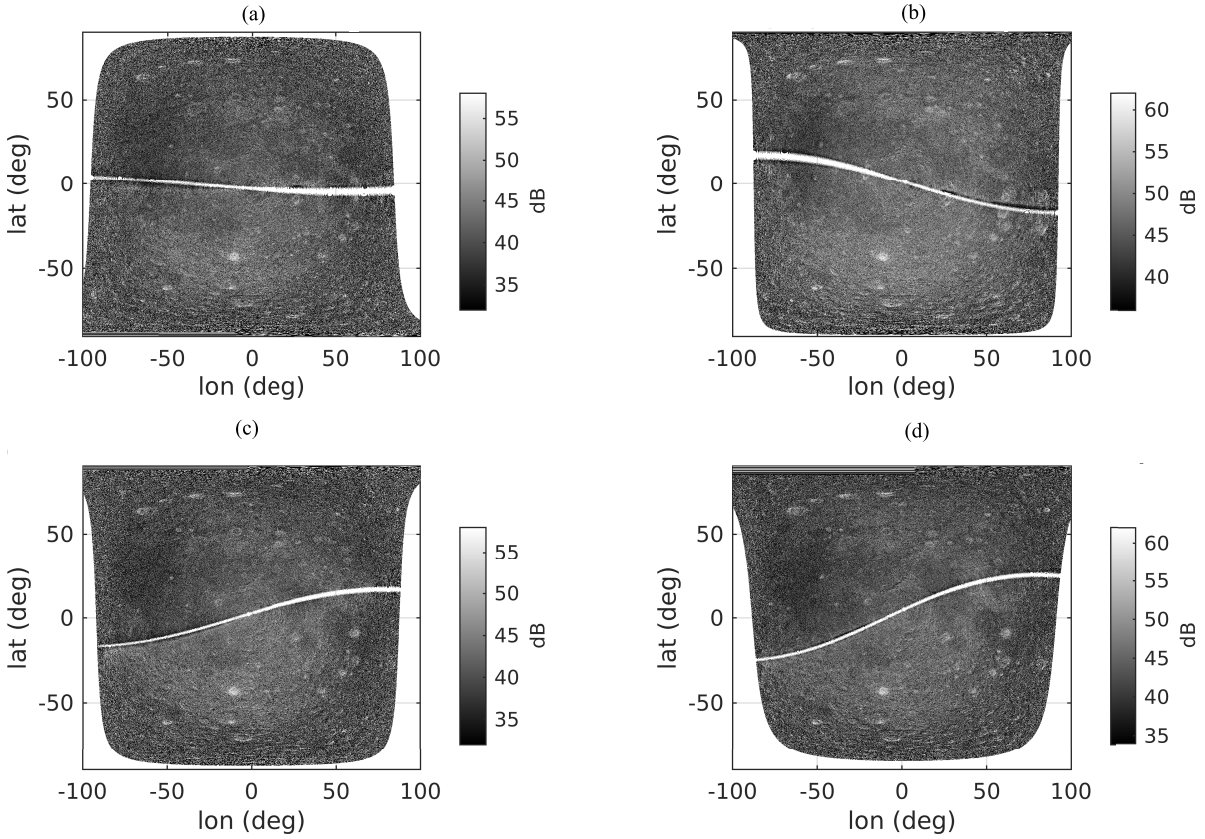

Fig. 5. Mosaic images of the northern and southern hemispheres of the nearside of the Moon. They are LFM chirp results. They are in the lunar projection coordinate system, i.e., latitude and longitude coordinate system. The longitude range is 100°W–100°E, the step length is 0.05°, the latitude range is 90°S–90°N, and the step length is 0.05°. (a) One-look result during 01:00–01:30 LT on January 27, 2021. (b) One-look result during 09:15–09:45 LT on February 7, 2021. (c) One-look result during 19:15–19:45 LT on February 19, 2021. (d) One-look result during 14:30–15:00 LT on March 16, 2021. The blank area though the longitude direction is the Doppler equator area. Near this area, there is still a slight "north–south ambiguity" due to the second problem of the mosaic technique we used mentioned in Section V-B. (a) January 26, 2021 lunar image (lon-lat). (b) February 7, 2021 lunar image (lon-lat). (c) February 19, 2021 lunar image (lon-lat). (d) March 16, 2021 lunar image (lon-lat).

needed at least to receive the echo at the same time. Also, the echo from north–south ambiguity points on lunar surface can be distinguished by using the phase difference arising from different electrical path lengths between the reflecting areas and the two antennas [15]. Therefore, it is necessary to apply interferometry to solve the problem of north–south ambiguity in follow-up work.

To address the second problem, we propose the following two inequalities:

$$(\theta_0 - \theta_{3\text{dB}})/2 < \emptyset_{\text{moon}} \tag{10}$$

$$(\theta_0 - \theta_{10\text{dB}})/2 < \emptyset_{\text{moon}} \tag{11}$$

where θ_0 is the first null beamwidth, $\theta_{3\text{dB}}$ is the 3-dB beamwidth, $\theta_{10\text{dB}}$ is the 10-dB beamwidth, and $\emptyset_{\text{moon}}$ is the field-of-view angle corresponding to the lunar radius of approximately 0.25°. We suggest that if the beamwidth of a radar satisfies inequality (10), there is no need to consider the tradeoff problem and the first null beamwidth can be directly used in the experiment. If inequality (10) is not satisfied, but inequality (11) is satisfied, the first null beamwidth can still be considered, but some other methods, such as increasing the pulselength, need to be applied to compensate for the weaker SNR. If inequalities (10) and (11) are not satisfied, the compromise problem needs to be considered. In this situation, a 10-dB beamwidth can be used to design an experiment.

C. Lunar Maps in Lunar Projection Coordinate System Obtained by Chirp Experiment

To obtain a 500-m range resolution, we used a 0.3-MHz bandwidth chirp pulse in lunar imaging experiments. To compensate for the wasted energy in the beam main lobe and ensure sufficient SNR when only the northern or the southern hemisphere is illuminated, we chose a relatively long pulselength of 2 ms whenever that was possible. From December 2020 to March 2021, 21 chirp imaging experiments were conducted. Each image was generated with a coherent integration time of 4 min.

1) Imaging the Whole Region of the Nearside of the Moon: Fig. 5 shows four lunar maps in the lunar projection coordinate system, i.e., latitude and longitude coordinate systems. They are one-look results. They are generated from the four experiments on the same date, as shown in Fig. 4. These lunar maps are mosaic of the northern and southern hemispheres of the nearside of the Moon. The image is a lunar OCP echo image. It has been corrected for the influence of the incident angle of the radar wave, the area of the scattering element, and the antenna pattern. Therefore, the information indicated

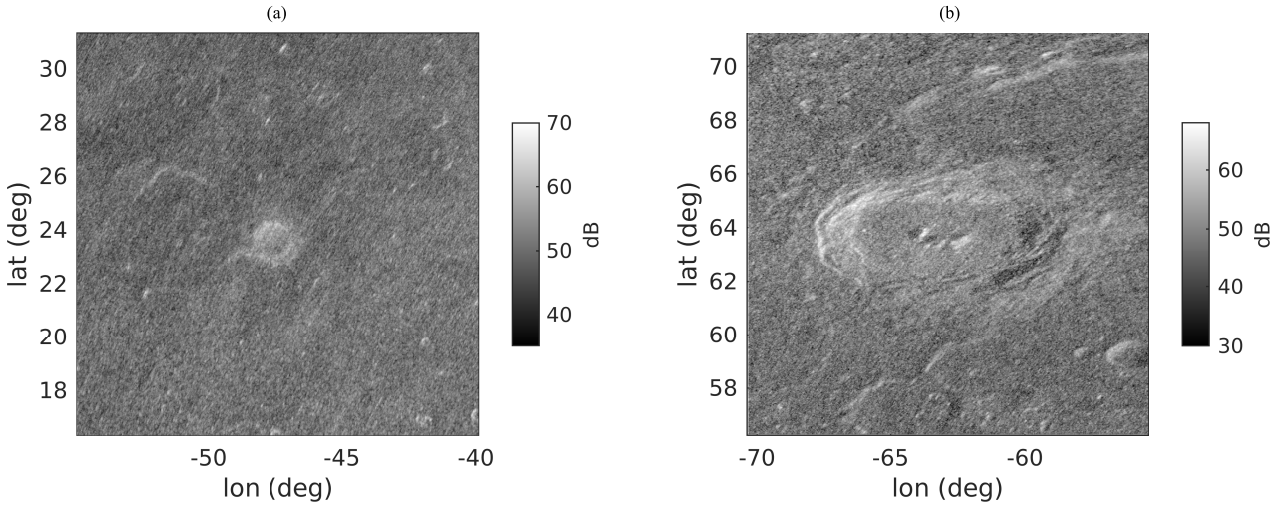

Fig. 6. Lunar local images. (a) Aristarchus crater region radar map. The longitude range is 54.9°W–39.9°W, the latitude range is 16.3°N–31.3°N, and the grid step is 0.01°. The resolution is approximately 0.65 km × 1.55 km. (b) Pythagoras crater region radar map. The longitude range is 70.4°W–55.4°W, the latitude range is 56.2°N–71.2°N, and the grid step is 0.01°. The resolution is approximately 0.52 km × 1.25 km. They were obtained by averaging 32 looks. (a) Aristarchus crater (32 looks averaged). (b) Pythagoras crater (32 looks averaged).

by the variation in the SNR in Fig. 5 mainly includes the Moon surface and the subsurface (at a depth of 5–10 m) rock abundance for diameters on the decimeter-to-meter scale, the slope of the terrain, the dielectric properties, and other factors.

2) Imaging of Local Areas on the Moon: Two local areas, Aristarchus crater and Pythagoras crater, were imaged and are shown in Fig. 6. The local resolution is approximately 0.65 km × 1.55 km for Aristarchus crater region and 0.52 km × 1.25 km for Pythagoras crater region. We chose six experiments that showed better imaging quality from all the chirp experiments. Also, each experiment generated 4–6 lunar maps. Therefore, we got 32 looks with relatively high imaging quality. In Fig. 6, the two images were derived from multilook averaging of these 32 looks. Theoretically, the noise variance of the multilook averaging result is $1/(32)^{1/2} \approx 0.18$ times that of a one-look result. Due to this, the noise speckle is suppressed in multilook averaging images.

VI. Conclusion

This article introduces the lunar imaging experiments and results using SYISR in detail. Two waveforms were used, including 13-bit Barker coded pulse and LFM chirp pulse. The RD algorithm was used to process the signal and obtain the RD lunar map. The resolutions are shown in Table I. With the coordinate projection method, the lunar images in the observation Cartesian coordinate system (Fig. 4) and the lunar projection coordinate system (Fig. 5) were obtained. In addition, two images of local areas on the Moon, which are the results after the multilook averaging process, were generated (Fig. 6).

The IF decoding method was adopted to reduce the sidelobe effect of 13-bit Barker code MF method. The IF result indicated that some pollution in range direction still exists. The reasons are not clear now and we need to do further study. However, IF decoding is still helpful in the case of two-phase encoding that is used for lunar imaging experiment.

Mosaic imaging of northern and southern hemispheres of the nearside of the Moon was used to reduce the north–south ambiguity. Actually, this method is not entirely suitable to apply to SYISR because the relatively large beamwidth of the instrument cannot completely solve the north–south ambiguity and ensure the beam-pattern power at the same time. However, we found a compromise to apply it with a trade between north–south ambiguity and overall beam-pattern power. We discuss the disadvantages of this compromised way in Section V-B. In the future, SYISR will upgrade into a tristatic system, and then, the interferometry can be used to solve the north–south ambiguity.

This article is an introduction and summary of the experiment design and data processing techniques for the SYISR lunar imaging experiments. Due to the fact that only the OCP echo was received, what we can do for the lunar science is limited. However, our work proves the ability of detecting and imaging the Moon using SYISR. In the future, collaborating with another antenna that can receive OCP and SCP echo at the same time, it is possible that more research work can be carried out. This includes modeling of the radar echoes from the lunar surface and subsurface, estimating crater ages and regolith thickness [1], studying the geologic evolution of the Moon [2], and searching for ice in polar craters [34].

In addition, in future work if the coherent integration time increase to give better resolution (azimuth resolution better than 0.8 km), the focusing algorithm need to be adopted. Actually, we have also done some study on focusing algorithm recently. We proposed the use of the back projection algorithm to obtain focused lunar images to solve this problem [35].

References

[1] W. Fa and M. A. Wieczorek, "Regolith thickness over the lunar nearside: Results from Earth-based 70-cm Arecibo radar observations," *Icarus*, vol. 218, no. 2, pp. 771–787, 2012, doi: 10.1016/j.icarus.2012.01.010.

[2] B. A. Campbell, B. Ray Hawke, G. A. Morgan, L. M. Carter, D. B. Campbell, and M. Nolan, "Improved discrimination of volcanic complexes, tectonic features, and regolith properties in mare serenitatis from Earth-based radar mapping," *J. Geophys. Res., Planets*, vol. 119, no. 2, pp. 313–330, Feb. 2014, doi: 10.1002/2013JE004486.

[3] T. W. Thompson, "A review of Earth-based radar mapping of the Moon," *Moon Planets*, vol. 20, no. 2, pp. 179–198, 1979, doi: 10.1007/BF00898069.

[4] B. A. Campbell *et al.*, "Earth-based 12.6-cm wavelength radar mapping of the Moon: New views of impact melt distribution and mare physical properties," *Icarus*, vol. 208, no. 2, pp. 565–573, 2010, doi: 10.1016/j.icarus.2010.03.011.

[5] N. J. S. Stacy, D. B. Campbell, and P. G. Ford, "Arecibo radar mapping of the lunar poles: A search for ice deposits," *Science*, vol. 276, no. 5318, pp. 1527–1530, Jun. 1997, doi: 10.1126/science.276.5318.1527.

[6] S. Zisk, "Mare Crisium area topography: A comparison of earth-based radar and Apollo mapping camera results," in *Mare Crisium: The View From Lunar 24*. New York, NY, USA: Pergamon, 1978, pp. 75–80.

[7] T. Hagfors, "Remote probing of the Moon by infrared and microwave emissions and by radar," *Radio Sci.*, vol. 5, no. 2, pp. 189–227, 1970, doi: 10.1029/RS005i002p00189.

[8] G. H. Pettengill and J. C. Henry, "Enhancement of radar reflectivity associated with the lunar Crater tycho," *J. Geophys. Res.*, vol. 67, no. 12, pp. 4881–4885, Nov. 1962, doi: 10.1029/JZ067i012p04881.

[9] G. H. Pettengill, S. H. Zisk, and T. W. Thompson, "The mapping of lunar radar scattering characteristics," *Moon*, vol. 10, no. 1, pp. 3–16, May 1974, doi: 10.1007/BF00562016.

[10] T. W. Thompson, "Atlas of lunar radar maps at 70-cm wavelength," *Moon*, vol. 10, no. 1, pp. 51–85, May 1974, doi: 10.1007/BF00562018.

[11] S. H. Zisk, G. H. Pettengill, and G. W. Catuna, "High-resolution radar maps of the lunar surface at 3.8-cm wavelength," *Moon*, vol. 10, no. 1, pp. 17–50, May 1974, doi: 10.1007/BF00562017.

[12] T. W. Thompson, H. Masursky, R. W. Shorthill, G. L. Tyler, and S. H. Zisk, "A comparison of infrared, radar, and geologic mapping of lunar craters," *Moon*, vol. 10, no. 1, pp. 87–117, May 1974, doi: 10.1007/BF00562019.

[13] C. C. Counselman, H. F. Hinteregger, and I. I. Shapiro, "Astronomical applications of differential interferometry," *Science*, vol. 178, no. 4061, pp. 607–608, Nov. 1972, doi: 10.1126/science.178.4061.607.

[14] S. H. Zisk, "A new, Earth-based radar technique for the measurement of lunar topography," *Moon*, vol. 4, nos. 3–4, pp. 296–306, 1972, doi: 10.1007/BF00561997.

[15] T. W. Thompson, "Map of lunar radar reflectivity at 7.5-m wavelength," *Icarus*, vol. 13, no. 3, pp. 363–370, Nov. 1970, doi: 10.1016/0019-1035(70)90086-2.

[16] J. Vierinen and M. S. Lehtinen, "32-cm wavelength radar mapping of the Moon," in *Proc. Eur. Radar Conf. (EuRAD)*, Sep./Oct. 2009, pp. 222–225.

[17] T. W. Thompson, "High-resolution lunar radar map at 70-cm wavelength," *Earth, Moon Planets*, vol. 37, no. 1, pp. 59–70, Jan. 1987, doi: 10.1007/BF00054324.

[18] B. A. Campbell *et al.*, "Focused 70-cm wavelength radar mapping of the Moon," *IEEE Trans. Geosci. Remote Sens.*, vol. 45, no. 12, pp. 4032–4042, Dec. 2007, doi: 10.1109/TGRS.2007.906582.

[19] J. Vierinen, T. Tveito, B. Gustavsson, S. Kesaraju, and M. Milla, "Radar images of the Moon at 6-meter wavelength," *Icarus*, vol. 297, pp. 179–188, Nov. 2017, doi: 10.1016/j.icarus.2017.06.035.

[20] B. Campbell and D. Campbell, "Regolith properties in the south polar region of the Moon from 70-cm radar polarimetry," *Icarus*, vol. 180, no. 1, pp. 1–7, Jan. 2006, doi: 10.1016/j.icarus.2005.08.018.

[21] B. A. Campbell, "Planetary geology with imaging radar: Insights from Earth-based lunar studies, 2001–2015," *Publications Astronomical Soc. Pacific*, vol. 128, no. 964, 2016, Art. no. 062001, doi: 10.1088/1538-3873/128/964/062001.

[22] W. Fa and Y. Cai, "Circular polarization ratio characteristics of impact craters from mini-RF observations and implications for ice detection at the polar regions of the Moon," *J. Geophys. Res. Planets*, vol. 118, no. 8, pp. 1582–1608, 2013, doi: 10.1002/jgre.20110.

[23] J. K. Harmon, M. C. Nolan, D. I. Husmann, and B. A. Campbell, "Arecibo radar imagery of Mars: The major volcanic provinces," *Icarus*, vol. 220, no. 2, pp. 990–1030, Aug. 2012, doi: 10.1016/j.icarus.2012.06.030.

[24] B. A. Campbell *et al.*, "The mean rotation rate of Venus from 29 years of Earth-based radar observations," *Icarus*, vol. 332, pp. 19–23, Nov. 2019, doi: 10.1016/j.icarus.2019.06.019.

[25] C. D. Neish, D. T. Blewett, J. K. Harmon, E. I. Coman, J. T. S. Cahill, and C. M. Ernst, "A comparison of rayed craters on the Moon and Mercury," *J. Geophys. Res., Planets*, vol. 118, no. 10, pp. 2247–2261, Oct. 2013, doi: 10.1002/jgre.20166.

[26] K. J. Lawrence *et al.*, "Arecibo and goldstone radar images of near-Earth asteroid (469896) 2005 WC1," *Icarus*, vol. 300, pp. 12–20, Jan. 2018, doi: 10.1016/j.icarus.2017.08.028.

[27] E. L. Key, E. N. Fowle, and R. D. Haggart, "A method of side-lobe suppression in phase-coded pulse compression systems," MIT Lincoln Lab., Tech. Rep. 209, Cambridge, MA, USA, 1959.

[28] M. P. Sulzer, "Recent incoherent scatter techniques," *Adv. Space Res.*, vol. 9, no. 5, pp. 153–162, Jan. 1989, doi: 10.1016/0273-1177(89)90353-0.

[29] M. Lehtinen *et al.*, "A new incoherent scatter technique in the EISCAT svalbard radar," *Radio Sci.*, vol. 37, no. 4, pp. 3-1–3-14, Aug. 2002.

[30] M. S. Lehtinen, B. Damtie, and T. Nygrén, "Optimal binary phase codes and sidelobe-free decoding filters with application to incoherent scatter radar," *Annales Geophysicae*, vol. 22, no. 5, pp. 1623–1632, Apr. 2004.

[31] D. F. Winter, "A theory of radar reflections from a rough Moon," *J. Res. Nat. Bur. Standards, D, Radio Propag.*, vol. 66D, no. 3, p. 215, May 1962, doi: 10.6028/jres.066D.025.

[32] M. Li *et al.*, "Simulation of the signal-to-noise ratio of Sanya incoherent scatter radar tristatic system," *IEEE Trans. Geosci. Remote Sens.*, vol. 59, no. 4, pp. 2982–2993, Apr. 2021, doi: 10.1109/TGRS.2020.3008427.

[33] T. Yu, M. Li, C. Xia, X. Zuo, Z. Liu, and B. Zhao, "A new method for deriving equatorial plasma bubble velocity by tracing OI 630 nm all-sky images," *J. Geophys. Res., Space Phys.*, vol. 123, no. 11, pp. 9619–9633, 2018, doi: 10.1029/2018JA025332.

[34] W. Fa and Y. Cai, "Circular polarization ratio characteristics of impact craters from mini-RF observations and implications for ice detection at the polar regions of the Moon," *J. Geophys. Res., Planets*, vol. 118, no. 8, pp. 1582–1608, 2013, doi: 10.1002/jgre.20110.

[35] M. Li *et al.*, "Focused lunar imaging experiment using the back projection algorithm based on sanya incoherent scatter radar," *Remote Sens.*, 2022.